

# Efficient Simulation of Non-Markovian Path Integrals via Imaginary Time Evolution of an Effective Hamiltonian

Xiaoyu Yang,<sup>1</sup> Limin Liu,<sup>1</sup> Wencheng Zhao,<sup>1</sup> Jiajun Ren,<sup>1, a)</sup> and Wei-Hai Fang<sup>1</sup>

*Key Laboratory of Theoretical and Computational Photochemistry,*

*Ministry of Education, College of Chemistry, Beijing Normal University,*

*100875 Beijing, People's Republic of China.*

Accurately simulating the non-Markovian dynamics of open quantum systems remains a significant challenge. While the recently proposed time-evolving matrix product operator (TEMPO) algorithm based on path integrals successfully circumvents the exponential scaling associated with memory length, its reliance on layer-by-layer tensor contractions and compressions leads to steep scaling with respect to the system Hilbert space dimension. In this work, we introduce the effective Hamiltonian-based TEMPO (EH-TEMPO) algorithm, which reformulates the calculation of the Feynman-Vernon influence functional as an imaginary time evolution governed by an effective Hamiltonian. We demonstrate that this effective Hamiltonian admits a highly compact matrix product operator representation, enabling substantial compression with negligible loss of accuracy. Combining a one-shot global evolution with a backward retrieval approach, EH-TEMPO significantly reduces algorithmic complexity and is naturally suited for GPU acceleration. We benchmark the method against the process tensor TEMPO algorithm using the 7-site Fenna-Matthews-Olson complex model. The results demonstrate that EH-TEMPO achieves numerically exact accuracy with superior efficiency, delivering speedups of up to 17.5 $\times$  on GPU hardware compared to standard CPU implementations.

---

<sup>a)</sup>Electronic mail: jjren@bnu.edu.cn

## I. INTRODUCTION

The study of quantum dynamics in condensed-phase systems<sup>1,2</sup> is central to understanding a wide range of physical and chemical phenomena, including carrier transport in organic semiconductors and excitation energy transfer in photosynthetic complexes. In these systems, the phonon environment affects the electronic dynamics through electron-phonon interactions, inducing decoherence and energy dissipation that ultimately govern the overall functional properties.<sup>3–5</sup>

Various approaches have been developed to simulate such electron-phonon coupled dynamics.<sup>6</sup> The first category treats the composite system, which comprises both electronic and phononic degrees of freedom, as a closed quantum system by explicitly propagating the full wavefunction according to the Schrödinger equation. Prominent examples include the time-dependent density matrix renormalization group (TD-DMRG),<sup>7,8</sup> tree tensor network states (TTNS),<sup>9,10</sup> and the multilayer multi-configuration time-dependent Hartree (ML-MCTDH) approach.<sup>11,12</sup> While these methods offer high accuracy and are robust across broad parameter regimes, their computational cost increases rapidly with the number of bath modes, often rendering long-time simulations of realistic condensed-phase problems prohibitively expensive. The second category focuses on the reduced dynamics of the system of interest by tracing out the phononic degrees of freedom. This includes perturbative approaches based on quantum master equations, such as the Lindblad<sup>13,14</sup> and Redfield equations,<sup>15,16</sup> which commonly invoke the Markov approximation. However, capturing non-Markovian memory effects, which are essential in many chemical systems, requires numerically exact methods. The most notable among these are the hierarchical equations of motion (HEOM),<sup>17,18</sup> non-Markovian quantum state diffusion (NMQSD),<sup>19,20</sup> and the quasi-adiabatic propagator path integral (QuAPI).<sup>21,22</sup>

QuAPI, originally developed by Makri and coworkers, can in principle fully retain non-Markovian effects and handle arbitrary bath spectral densities at both zero and finite temperatures.<sup>21–24</sup> However, the computational cost and storage requirements of the practical iterative QuAPI algorithm scale exponentially with the memory time, limiting its applicability to small systems or short memory times. Recently, tensor network (TN) algorithms have been applied to enhance path integral methods.<sup>25–27</sup> A significant breakthrough was achieved with the introduction of the time-evolving matrix product operator (TEMPO) algo-

rithm proposed by Strathearn *et al.*<sup>25</sup> TEMPO combines the influence functional formalism with TN techniques, specifically matrix product states (MPS) and matrix product operators (MPO),<sup>28</sup> by expressing the influence functional as the contraction of a two-dimensional TN. This reduces the scaling with respect to memory length from exponential to polynomial, enabling efficient simulations of long-time non-Markovian dynamics. Subsequent developments have significantly extended the generality and capability of TEMPO, including reformulations within the process tensor (PT) framework for multi-time correlation functions,<sup>29</sup> extensions to general off-diagonal or non-commuting system-bath couplings,<sup>30–32</sup> generalizations to equilibrium initial states<sup>33</sup> and fermionic baths,<sup>34,35</sup> and combinations with other powerful algorithms such as the small matrix path integral<sup>36,37</sup> and high-dimensional tensor networks.<sup>38</sup>

Despite these successes, the standard TEMPO algorithm still faces significant challenges when applied to multi-state systems. A key step in TEMPO is the iterative contraction and compression of the layered MPOs representing the incremental influence functional.<sup>25</sup> In general, the bond dimension of the MPOs grows quadratically with the system Hilbert space dimension  $d$ , making standard singular value decomposition (SVD)-based compression prohibitively expensive for multi-state systems (scaling as  $O(d^7)$  when forward and backward path indices are separated, or  $O(d^8)$  otherwise). Additionally, constructing a compact MPO for the influence functional of general system-bath interactions manually is non-trivial and laborious, and existing automated MPO construction algorithms<sup>39–41</sup> are incompatible with the influence functional form, which lacks a simple sum-of-products (SOP) structure. In this work, we propose an effective Hamiltonian-based TEMPO (EH-TEMPO) algorithm to address the scalability of (PT-)TEMPO for multi-state systems. Instead of the standard layer-by-layer contraction and compression scheme, we derive the influence functional via the imaginary time evolution of an effective Hamiltonian. This reformulation offers three distinct advantages over the original (PT-)TEMPO algorithm: (i) The effective Hamiltonian takes an SOP form, enabling the use of automated MPO construction algorithms to generate optimal MPO representations for arbitrary system-bath couplings with minimal bond dimensions. (ii) Well-established time evolution algorithms, such as those based on the time-dependent variational principle (TDVP),<sup>42,43</sup> can be employed to obtain the overall influence functional in a one-shot calculation with relatively large time steps, replacing the costly layer-by-layer heavy calculations. The computational scaling with respect to the

system Hilbert space dimension  $d$  reduces to  $O(d^2)$ . (iii) With TDVP based time evolution algorithms, the EH-TEMPO algorithm avoids decompositions of large tensors, making it highly amenable to GPU acceleration. We benchmark the EH-TEMPO algorithm by simulating excitation energy transfer dynamics in the 7-site Fenna-Matthews-Olson (FMO) complex. By comparing our results with those from the PT-TEMPO algorithm, we demonstrate that EH-TEMPO provides accurate influence functionals with superior computational efficiency for multi-state systems.

The remainder of this paper is organized as follows. Section II briefly reviews the theoretical foundations of the QuAPI and TEMPO algorithms and then details the proposed EH-TEMPO algorithm. In Section III, we systematically analyze the accuracy and efficiency of the EH-TEMPO method, comparing its performance against standard benchmarks. Finally, conclusions are presented in Section IV.

## II. METHODS

### A. The QuAPI and TEMPO Algorithms

A generic system-bath coupled problem is described by the total Hamiltonian:

$$\hat{H} = \hat{H}_S + \hat{H}_B + \hat{H}_{SB}, \quad (1)$$

$$\hat{H}_B = \sum_i \frac{1}{2} \hat{p}_i^2 + \frac{1}{2} \omega_i^2 \hat{q}_i^2, \quad (2)$$

$$\hat{H}_{SB} = \sum_n \hat{S}_n \otimes \sum_i c_{ni} \hat{q}_i, \quad (3)$$

where  $\hat{H}_S$  is the system Hamiltonian,  $\hat{H}_B$  is the bath Hamiltonian, and  $\hat{H}_{SB}$  describes the system-bath interaction. In this work, we restrict our consideration to diagonal system-bath coupling, for which there exists a basis  $\{|s\rangle\}$  that simultaneously diagonalizes all operators  $\hat{S}_n$ , with eigenvalues  $s$ . For notational conciseness, we consider a single coupling term in Eq. (3) in the following and thus omit the summation over  $n$ . The time evolution of the total density matrix is given by  $\hat{\rho}(t) = e^{-i\hat{H}t} \hat{\rho}(0) e^{i\hat{H}t}$ . We assume a factorized initial condition at  $t = 0$ ,  $\hat{\rho}(0) = \hat{\rho}_S(0) \otimes \hat{\rho}_B^{\text{eq}}$ , where the bath is in thermal equilibrium. The extension to correlated thermal equilibrium initial states is discussed in Refs. 33, 44, and 45. Applying the standard Trotter splitting of the short-time propagator  $e^{-i\hat{H}\Delta t}$  to separate system and

bath contributions, the reduced density matrix  $\hat{\rho}_S(t) = \text{Tr}_B[\hat{\rho}(t)]$  at time  $t = N_t \Delta t$  can be expressed as a discretized path integral:

$$\hat{\rho}_S(N_t \Delta t) = \sum_{s_0^\pm, \dots, s_{N_t-1}^\pm} \langle s_0^\pm | \hat{\rho}_s(0) | s_0^- \rangle G(s_0^\pm, \dots, s_{N_t}^\pm) F(s_1^\pm, \dots, s_{N_t}^\pm). \quad (4)$$

Here,  $s_0^\pm, s_1^\pm, \dots, s_{N_t}^\pm$  denote the discretized forward (+) and backward (−) system paths. The system propagator  $G$  is given by the product of short-time propagators:

$$G(s_0^\pm, \dots, s_{N_t}^\pm) = \prod_{k=1}^{N_t} \langle s_k^+ | e^{-i\hat{H}_0 \Delta t} | s_{k-1}^+ \rangle \langle s_{k-1}^- | e^{i\hat{H}_0 \Delta t} | s_k^- \rangle, \quad (5)$$

where  $\hat{H}_0$  is the QuAPI-type shifted system Hamiltonian along the adiabatic path.<sup>23</sup> The environmental effects are encoded in the Feynman-Vernon influence functional  $F$ , which accounts for non-Markovian memory effects.<sup>46</sup> For a Gaussian bath with linear coupling,  $F$  takes the form:<sup>21</sup>

$$F(s_1^\pm, \dots, s_{N_t}^\pm) = \prod_{k=1}^{N_t} \prod_{k'=1}^k I_{\Delta k}(s_{k'}^\pm, s_k^\pm), \quad \Delta k = k - k', \quad (6)$$

$$I_{\Delta k}(s_{k'}^\pm, s_k^\pm) = \exp [-(s_k^+ - s_k^-)(\eta_{kk'} s_{k'}^+ - \eta_{kk'}^* s_{k'}^-)].$$

The coefficients  $\eta_{kk'}$  are determined by the bath spectral density and the temperature. For simplicity, we present expressions based on first-order Trotter splitting. The extension to second-order splitting is straightforward.<sup>21,22</sup>

Computing Eq. (4) exactly incurs an exponential cost with respect to the memory length. To overcome this challenge, the TEMPO algorithm identifies the discrete path variables  $s_k^{pm}$  as the physical indices of a tensor network. The incremental influence functional in Eq. (7) can be compactly represented as a one-dimensional MPO (after inserting Kronecker deltas with respect to  $s_k^\pm$ ):

$$f_k(s_1^\pm, \dots, s_k^\pm) = \prod_{k'=1}^k I_{\Delta k}(s_{k'}^\pm, s_k^\pm), \quad (7)$$

$$\hat{B}_k = \left( \prod_{k'=1}^{k-1} \delta_{i_{k'}^+}^{s_{k'}^+} \delta_{i_{k'}^-}^{s_{k'}^-} \right) f_k = \sum_{\{a\}} B[1]_{a_1}^{s_1^\pm, i_1^\pm} \dots B[k-1]_{a_{k-2} a_{k-1}}^{s_{k-1}^\pm, i_{k-1}^\pm} B[k]_{a_{k-1}}^{s_k^\pm}, \quad (8)$$

Here,  $a_i$  is the index linking adjacent matrices, the size of which is called the bond dimension. The overall influence functional thus exhibits a two-dimensional triangular structure, which is contracted as a sequence of layered MPOs to yield a final MPS (see Fig. 1(a)):

$$F(s_1^\pm, \dots, s_{N_t}^\pm) = \hat{B}_{N_t} \hat{B}_{N_t-1} \dots \hat{B}_1. \quad (9)$$

In practice, after successively contracting adjacent layers, standard SVD-based compression is applied to truncate the bond dimension of MPS by discarding renormalized states with small singular values, thereby circumventing the exponential scaling of computational cost and storage with respect to  $N_t$ .

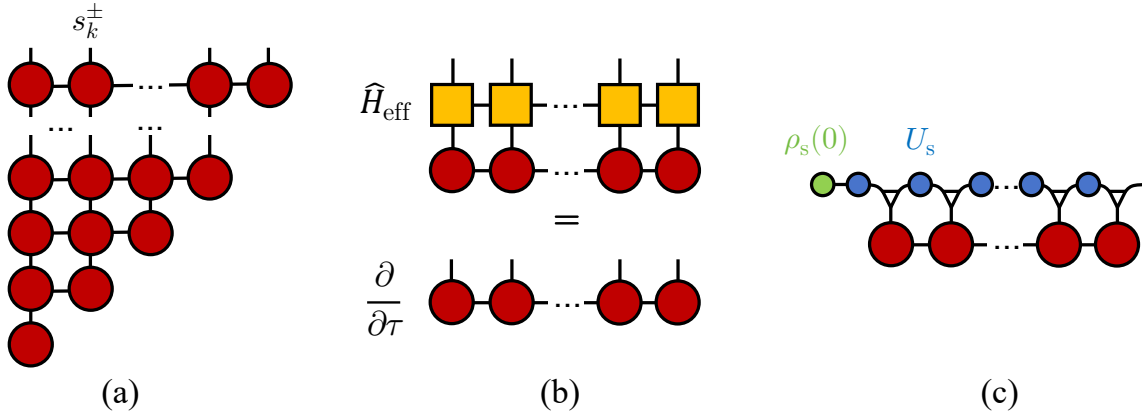


FIG. 1. Tensor network diagrams for the TEMPO algorithms. (a) The triangular tensor network representation of the influence functional used in the (PT-)TEMPO algorithm. (b) The core algorithm of EH-TEMPO, where the influence functional is generated via the time evolution governed by the effective Hamiltonian MPO ( $\hat{H}_{\text{eff}}$ ). (c) The final tensor contraction to obtain the reduced density matrix, combining the influence functional MPS with the system propagators  $U_S$  and the initial state  $\rho_S(0)$ . The white triangle represents  $\delta_{ijk}$ .

In the original TEMPO algorithm,<sup>25</sup> starting from the system initial state  $\rho_S(0)$ , the one-step system propagator is absorbed into the pairwise influence functional with  $\Delta k = 1$  during the contraction. Consequently, instead of obtaining the overall influence functional, the so-called augmented density tensor (ADT), which is the summand in Eq. (4), is obtained directly. The subsequent combination with the PT framework<sup>29</sup> enables the system propagator to be separated from the influence functional construction. This PT-TEMPO algorithm prevents the system propagators from participating in the SVD compression, resulting in higher accuracy for a given bond dimension in our experience. Moreover, PT-TEMPO allows reuse of the process tensor for different system Hamiltonians and operations, and is especially well suited for computing multi-time correlation functions. The trade-off is that the index of each local matrix must in general be doubled,  $s_k \rightarrow (s_k, s'_k)$ , which inevitably increases the computational cost. Fortunately, this doubling can be avoided for the diagonal

system-bath interaction considered in this work, making the computational cost of PT-TEMPO comparable to that of TEMPO. Once the overall influence functional is obtained in MPS form, the system reduced density matrix is readily computed by contracting with the system propagators and initial state (see Fig. 1(c)).

We now analyze the computational scaling of TEMPO and PT-TEMPO for diagonal system-bath couplings. In our implementation, the forward and backward index variables are separated as  $s_1^+, s_1^-, s_2^+, s_2^-, \dots, s_{N_t}^+, s_{N_t}^-$  rather than  $s_1^\pm, s_2^\pm, \dots, s_{N_t}^\pm$ , which doubles the number of sites but reduces the per-site cost. In the equations and figures presented in this paper, however, we group the forward and backward indices into a single site for clarity. The computational complexity of a two-layer contraction is  $O(N_t M_O^2 M_S^2 d^2)$ , where  $M_O$  is the bond dimension of the MPO in Eq. (8),  $M_S$  is the bond dimension of the MPS representing the overall influence functional (PT-TEMPO) or ADT (TEMPO),  $d$  is the system Hilbert space dimension, and  $N_t$  is the number of time steps. After contraction, the scaling of tensor decomposition and compression based on QR and SVD is  $O(N_t M_S^3 M_O^3 d)$ .<sup>43</sup> Since the optimal  $M_O$  scales as  $O(d^2)$  and there are  $N_t$  layers, the overall cost is  $O(N_t^2 M_S^2 d^6)$  for contractions and  $O(N_t^2 M_S^3 d^7)$  for decompositions. The standard TEMPO and PT-TEMPO algorithms thus exhibit steep scaling with respect to the system dimension  $d$ , which prohibits the efficient treatment of multi-state dynamics. Additionally, manual construction of the MPOs for the incremental influence functional in Eq. (8) is non-trivial and laborious. For example, in Ref. 25, it was found that for the spin-boson model, terms sharing the same factor  $(s_k^+ - s_k^-)$  can be merged to reduce  $M_O$ . Such detailed optimizations are important for efficient simulations but difficult to implement systematically, especially for complex system-bath couplings. These two limitations motivate the development of the EH-TEMPO algorithm presented in the next section.

## B. The EH-TEMPO Algorithm

The central idea of the EH-TEMPO algorithm is the reformulation of the influence functional as an imaginary time evolution (ITE) governed by an effective Hamiltonian  $\hat{H}_{\text{eff}}$ , which acts on the space of path indices  $|s_1\rangle \otimes |s_2\rangle \otimes \dots \otimes |s_{N_t}\rangle$ :

$$\hat{H}_{\text{eff}}^{N_t} = \sum_{k=1}^{N_t} \sum_{k'=1}^k (\hat{s}_k^+ - \hat{s}_k^-) (\eta_{kk'} \hat{s}_{k'}^+ - \eta_{kk'}^* \hat{s}_{k'}^-). \quad (10)$$

Here, the operators  $\hat{s}_k^\pm$  are diagonal in the path basis, satisfying  $\hat{s}_k^\pm|s_k^\pm\rangle = s_k^\pm|s_k^\pm\rangle$ . This effective Hamiltonian describes a one-dimensional lattice of length  $N_t$  along the temporal axis with long-range, complex-valued pairwise interactions  $\eta_{kk'}$  and  $\eta_{kk'}^*$ . For example, for a two-level system where  $s_k^\pm$  takes values  $\pm 1$ ,  $\hat{H}_{\text{eff}}$  is analogous to an Ising chain with long-range couplings. Since  $\hat{H}_{\text{eff}}$  takes the form of a sum of products, its MPO representation can be efficiently constructed using the automated bipartite graph algorithm developed in our previous works.<sup>10,40</sup> The bond dimension of the most compact MPO scales as  $O(N_t)$ , independent of  $d$ . To compute the state  $|\Psi_{\text{IF}}\rangle = \sum_{s_1^\pm, \dots, s_{N_t}^\pm} F(s_1^\pm, \dots, s_{N_t}^\pm)|s_1^\pm, \dots, s_{N_t}^\pm\rangle$ , which encodes the overall influence functional in its amplitudes, we start from an unnormalized initial state  $|\Psi_0\rangle$  representing an equal superposition of all path configurations. This state admits an MPS representation with  $M_S = 1$ :

$$|\Psi_0\rangle = \sum_{s_1^\pm, \dots, s_{N_t}^\pm} |s_1^\pm, \dots, s_{N_t}^\pm\rangle. \quad (11)$$

Then,  $|\Psi_{\text{IF}}\rangle$  can be calculated by solving the imaginary time Schrödinger equation from  $\tau = 0$  to  $\tau = 1$  under the effective Hamiltonian (see Fig 1(b)),

$$|\Psi_{\text{IF}}\rangle = e^{-\tau\hat{H}_{\text{eff}}}|\Psi_0\rangle, \quad \tau = 1. \quad (12)$$

In this work, we employ the standard TDVP-based projector splitting algorithm to perform the ITE.<sup>42,43</sup> This procedure yields the influence functional for the entire time history from  $t_1$  to  $t_{N_t}$  in a single MPS  $|\Psi_{\text{IF}}^{N_t}\rangle$ . In (PT-)TEMPO, if one regards each layer of MPO contraction as one time step, obtaining  $|\Psi_{\text{IF}}^{N_t}\rangle$  requires  $N_t$  steps. By contrast, the number of ITE steps  $N_\tau$  required in EH-TEMPO can be very small, typically from several to a dozen steps suffice, with  $N_\tau \ll N_t$ , as shown in the next section. This substantial reduction in the number of evolution steps translates directly into computational savings. Moreover, sophisticated adaptive time-step algorithms can be employed to further automate the ITE process, which is important for investigating unknown problems. Once  $|\Psi_{\text{IF}}^{N_t}\rangle$  is obtained, the reduced density matrix at the final time step  $t_{N_t}$  is computed as in PT-TEMPO (see Fig. 1(c)). However, a direct application of EH-TEMPO provides only the reduced density matrix at the final time step  $t_{N_t}$ . To obtain the full dynamical trajectory from  $t_1$  to  $t_{N_t}$ , three schemes can be employed:

1. **Independent scheme.** Perform ITE independently for  $\hat{H}_{\text{eff}}^1, \hat{H}_{\text{eff}}^2, \dots, \hat{H}_{\text{eff}}^{N_t}$  to obtain

$|\Psi_{\text{IF}}^1\rangle, |\Psi_{\text{IF}}^2\rangle, \dots, |\Psi_{\text{IF}}^{N_t}\rangle$  separately. Assuming  $N_\tau$  steps are required for each evolution to  $\tau = 1$ , this scheme requires  $N_t \cdot N_\tau$  ITE steps in total.

2. **Stepwise scheme.** Decompose  $\hat{H}_{\text{eff}}^{N_t}$  into a sum of incremental contributions  $\hat{h}_{\text{eff}}^k$  defined in Eq. (13), and perform ITE sequentially according to  $\hat{h}_{\text{eff}}^1, \hat{h}_{\text{eff}}^2, \dots, \hat{h}_{\text{eff}}^{N_t}$ , each from  $\tau = 0$  to  $\tau = 1$ :

$$\hat{h}_{\text{eff}}^k = \sum_{k'=1}^k (\hat{s}_k^+ - \hat{s}_k^-) (\eta_{k,k'} \hat{s}_{k'}^+ - \eta_{k,k'}^* \hat{s}_{k'}^-). \quad (13)$$

This approach closely parallels (PT-)TEMPO, with the key difference that the incremental influence functional is exactly and explicitly constructed in (PT-)TEMPO, whereas it is implicitly obtained through ITE in EH-TEMPO. This approach is also technically similar to that in Ref. 32, with the distinction that we adopt the effective Hamiltonian interpretation. Like the independent scheme, this requires  $N_t \cdot N_\tau$  ITE steps.

3. **Backward retrieval scheme.** All intermediate states  $|\Psi_{\text{IF}}^{n < N_t}\rangle$  are successively retrieved from  $|\Psi_{\text{IF}}^{N_t}\rangle$  by exploiting a property of the influence functional: when  $s_N^+ = s_N^-$ , the incremental influence functional  $f_N$  equals unity. This allows the influence functional to be retrieved backward:

$$|\Psi_{\text{IF}}^{N_t}\rangle \xrightarrow{s_{N_t}^+ = s_{N_t}^-} |\Psi_{\text{IF}}^{N_t-1}\rangle \xrightarrow{s_{N_t-1}^+ = s_{N_t-1}^-} \dots \xrightarrow{s_2^+ = s_2^-} |\Psi_{\text{IF}}^1\rangle. \quad (14)$$

Combined with this backward retrieval, only a one-shot evolution is needed, requiring just  $N_\tau$  ITE steps, which is significantly fewer than the preceding two schemes. The retrieval itself incurs negligible additional cost, involving only a single MPS sweep. However, since only  $|\Psi_{\text{IF}}^{N_t}\rangle$  is targeted in the one-shot calculation, the retrieval may introduce small errors.

The computational cost of EH-TEMPO is dominated by the ITE. Among the three schemes, the backward retrieval scheme is the most efficient and will be adopted in the numerical tests presented in Section III. Using the TDVP projector splitting method, the computational scaling is as follows:<sup>43</sup> the tensor contraction scales as  $O(N_\tau N_t (M_S^2 M_O^2 d^2 + M_S^3 M_O d))$ , and the tensor decomposition scales as  $O(N_\tau N_t M_S^3 d)$ . Compared to (PT-)TEMPO, the scaling with respect to the system dimension  $d$  is significantly reduced.

This constitutes the primary advantage of the EH-TEMPO algorithm. In addition, since EH-TEMPO avoids the decomposition of large tensors and the dominant operations are large tensor contractions, it is highly amenable to GPU parallelization, as demonstrated in Ref. 43. This leads to the significant speedups reported in Section III.

Furthermore, for a condensed-phase environment, the bath correlation function  $C(t)$  typically decays, so the long-range couplings  $\eta_{kk'}$  in  $\hat{H}_{\text{eff}}$  vanish for  $k - k' \gg \tau_{\text{mem}}/\Delta t$ , where  $\tau_{\text{mem}}$  is the memory time. This effective locality implies that the MPO representation of  $\hat{H}_{\text{eff}}$  can be efficiently compressed. In the next section, we find that after compression,  $M_O$  can be substantially smaller than the exact (uncompressed) value, yielding significant computational savings. This feature further underscores the effectiveness of the MPS representation for encoding the influence functional. In contrast to the fixed memory-length truncation used in QuAPI and TEMPO, where the memory effect is discarded beyond a specific time interval, the memory effect in EH-TEMPO is instead adaptively truncated according to singular values, similar in spirit to our previous work.<sup>47</sup> This compression strategy is effective at filtering out negligible memory contributions and provides more robust error control.

### III. RESULTS AND DISCUSSION

To evaluate the performance of the EH-TEMPO algorithm, we apply it to the widely used testbed, the excitation energy transfer dynamics in the 7-site Fenna-Matthews-Olson (FMO) complex described by the Frenkel-Holstein model. The Hamiltonian is:

$$\hat{H}_S = \sum_i \varepsilon_i \hat{a}_i^\dagger \hat{a}_i + \sum_{i \neq j} J_{ij} \hat{a}_i^\dagger \hat{a}_j, \quad (15)$$

$$\hat{H}_B + \hat{H}_{SB} = \sum_{i,\xi} \omega_\xi \hat{b}_{i\xi}^\dagger \hat{b}_{i\xi} + \sum_{i,\xi} g_{i\xi} \omega_\xi \hat{a}_i^\dagger \hat{a}_i (\hat{b}_{i\xi}^\dagger + \hat{b}_{i\xi}), \quad (16)$$

where  $\varepsilon_i$  is the site energy of pigment  $i$ , and  $J_{ij}$  is the excitonic coupling between pigments  $i$  and  $j$ . The parameters for  $\hat{H}_S$  are from Refs. 48 and 49. The bath is characterized by a Debye spectral density,  $J(\omega) = 2\lambda \frac{\omega \omega_c}{\omega^2 + \omega_c^2}$ , where  $\lambda$  is the reorganization energy and  $\omega_c$  is the cutoff frequency. For the 7-site FMO model with independent local baths, the influence functional generalizes Eq. (6) by taking the product over all site indices:

$$F(s_1^\pm, \dots, s_{N_t}^\pm) = \prod_{i=1}^7 \exp \left\{ - \sum_{k=1}^{N_t} \sum_{k'=1}^k (n_k^{i+} - n_k^{i-}) (\eta_{kk'} n_{k'}^{i+} - \eta_{kk'}^* n_{k'}^{i-}) \right\}, \quad (17)$$

where  $|s_k^\pm\rangle$  takes the local electronic state  $|i\rangle$  with  $i = 1, \dots, 7$ , and  $n_k^{i\pm}$  is the occupation number of site  $i$  at step  $k$ . The corresponding effective Hamiltonian is

$$\hat{H}_{\text{eff}} = \sum_{i=1}^7 \sum_{k=1}^{N_t} \sum_{k'=1}^k (\hat{n}_k^{i+} - \hat{n}_k^{i-}) (\eta_{kk'} \hat{n}_{k'}^{i+} - \eta_{kk'}^* \hat{n}_{k'}^{i-}), \quad (18)$$

where  $\hat{n}_k^{i\pm}$  is the occupation number operator satisfying  $\hat{n}_k^{i\pm} |s_k^\pm\rangle = \delta_{is} |s_k^\pm\rangle$ .

We benchmark EH-TEMPO against the numerically exact HEOM method and the PT-TEMPO algorithm. For the Debye spectral density, the HEOM method serves as an ideal benchmark. The accuracy of the population dynamics is quantified by the time-averaged cumulative deviation:

$$\mathcal{E}(\Delta t N_t) = \frac{1}{7N_t} \sum_{i=1}^7 \sum_{k=1}^{N_t} \left| P^{(i)}(k) - P_{\text{ref}}^{(i)}(k) \right|, \quad (19)$$

where  $P^{(i)}$  denotes the population of site  $i$ . We first verify the correctness of the EH-TEMPO algorithm. Fig. 2 displays the population dynamics at  $T = 77\text{K}$  with  $\lambda = 35\text{cm}^{-1}$  and  $\omega_c = 1/50\text{fs}^{-1}$ . The EH-TEMPO results employ a real-time step size  $\Delta t = 4\text{fs}$ , an adaptive imaginary time step (with relative tolerance  $10^{-5}$ ), and a bond dimension  $M_S = 128$ . The results show excellent agreement with the HEOM reference, capturing all oscillatory features of the coherent energy transfer dynamics.

In Fig. 3, we compare the error accumulation  $\mathcal{E}(t)$  of EH-TEMPO against PT-TEMPO. Two schemes are tested for EH-TEMPO: the backward retrieval scheme and the independent scheme. Both EH-TEMPO schemes maintain errors on the order of  $10^{-3}$ , comparable to PT-TEMPO at the same bond dimension  $M_S$ . Crucially, the backward retrieval scheme achieves accuracy similar to the much more expensive independent scheme, confirming that with a proper bond dimension the efficient backward retrieval introduces negligible additional error.

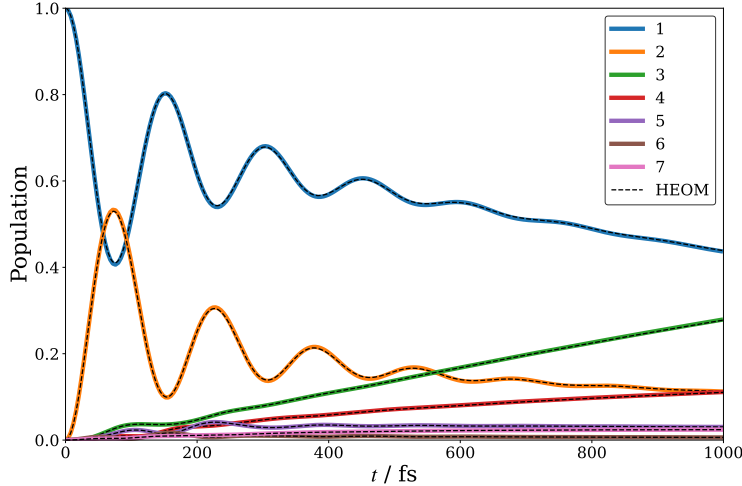


FIG. 2. Exciton population dynamics of the 7-site FMO complex at  $T = 77\text{ K}$ . The solid colored lines represent the results obtained via the EH-TEMPO algorithm (bond dimension  $M_S = 128$ ), while the dashed black lines denote the numerically exact HEOM reference. The two datasets are in excellent agreement, with the EH-TEMPO results accurately reproducing the detailed coherent oscillations.

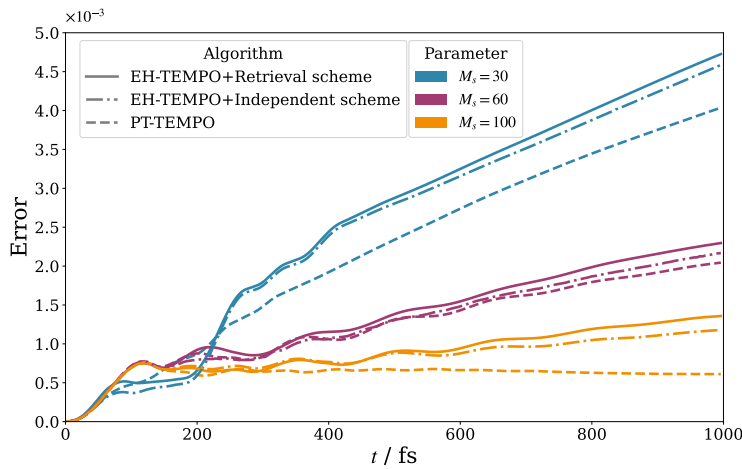


FIG. 3. Time evolution of the cumulative error  $\mathcal{E}(t)$  for the 7-site FMO complex. The performance of EH-TEMPO is compared against PT-TEMPO across three bond dimensions ( $M_S = 30, 60, 100$ ), represented by different colors. The line styles distinguish the algorithmic schemes: solid lines for EH-TEMPO with the backward retrieval scheme, dash-dotted lines for the independent scheme, and dashed lines for PT-TEMPO.

A key feature of EH-TEMPO is the compressibility of the effective Hamiltonian, which exploits the decay of the long-range couplings  $\eta_{kk'}$ . This allows the MPO representation of  $\hat{H}_{\text{eff}}$  to be compressed to save computational cost without significant loss of accuracy. Fig. 4 demonstrates this behavior. In panel (a), without compression ( $\eta = 0$ ), the bond dimension of MPO grows to 1752. By imposing an SVD truncation threshold  $\eta$ , the bond dimension is drastically reduced (e.g., to 20 for  $\eta = 10^{-4}$ ). Panel (b) shows that this aggressive compression incurs a minimal error penalty: even at  $\eta = 10^{-4}$ , the deviation from the uncompressed result remains negligible, with errors maintained on the order of  $10^{-3}$ .

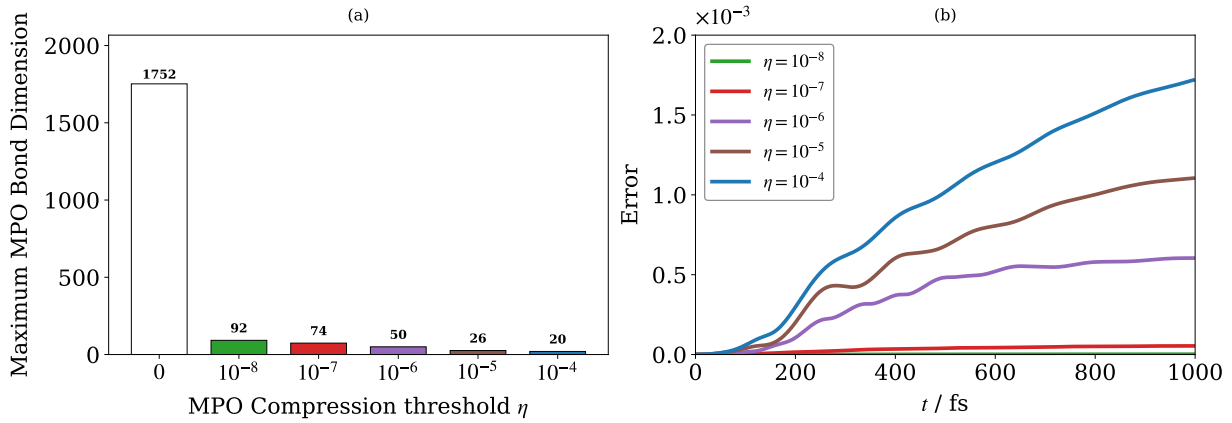


FIG. 4. Compressibility of the effective Hamiltonian MPO. (a) The maximum bond dimension of  $\hat{H}_{\text{eff}}$  as a function of the SVD compression threshold  $\eta$ . The bond dimension decreases drastically from the exact value (1752) to compact sizes ( $< 100$ ) with non-zero thresholds. (b) The time-dependent calculation error introduced by compression, relative to the uncompressed case. The error remains negligible (order of  $10^{-3}$ ) even for aggressive compression ( $\eta = 10^{-4}$ ).

The compressibility is further analyzed in Fig. 5 across different parameter regimes. As expected, slower bath dynamics (left panel,  $\omega_c$  from  $1/10 \text{ fs}^{-1}$  to  $1/100 \text{ fs}^{-1}$ ) and lower temperatures (right panel,  $T$  from 300 K to 10K) lead to larger MPO bond dimensions, reflecting longer memory times. Nevertheless, in all cases the compressed bond dimensions are orders of magnitude smaller than the uncompressed values (dashed lines), highlighting the effectiveness of compressing the effective Hamiltonian.

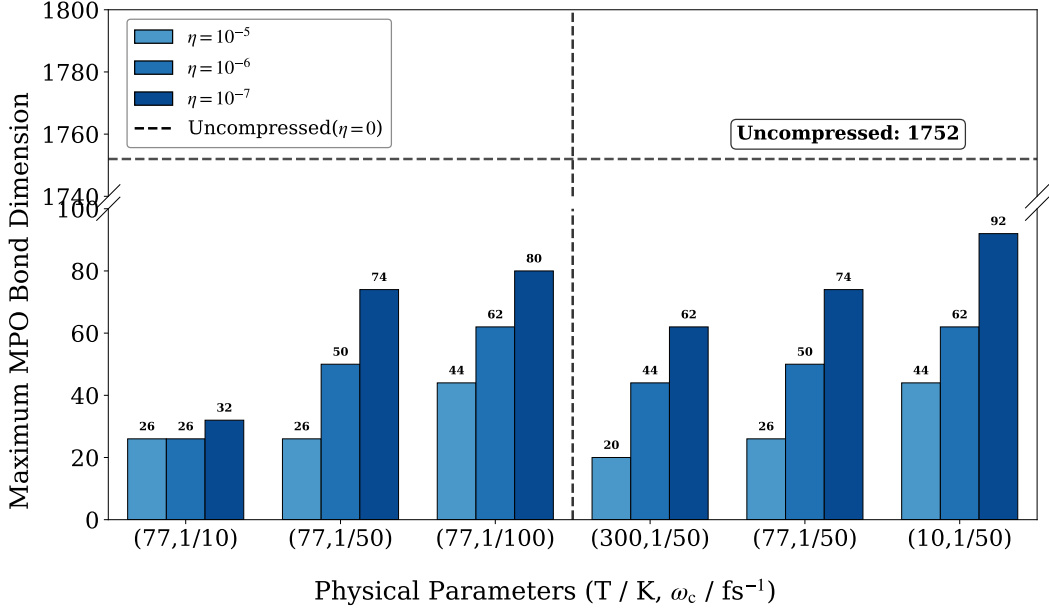


FIG. 5. Comparison of the maximum bond dimension of the effective Hamiltonian MPO with various physical parameters. The x-axis labels represent the parameter pairs ( $T/K, \omega_c/\text{fs}^{-1}$ ). The dashed line indicates the uncompressed bond dimension (1752), which is constant across these parameters for the given discretization. The colored bars show the significantly reduced bond dimensions after compression with thresholds  $\eta = 10^{-5}, 10^{-6}$  and  $10^{-7}$ , highlighting the efficiency of the compression across different temperatures and cutoff frequencies.

We next assess the convergence of the ITE in Fig. 6 with different step sizes. For fixed ITE step sizes  $d\tau = 1, 0.5, 0.2, 0.1/j$  ( $N_\tau = 1, 2, 5, 10$ , respectively), the error decreases with decreasing step size, as expected for the TDVP projector splitting algorithm. Notably, even with  $d\tau = 1/j$  ( $N_\tau = 1$ ), the error remains well controlled at the same order of magnitude ( $10^{-3}$ ). Furthermore, the adaptive step-size algorithm can be employed: with a relative tolerance of  $10^{-3}$  and an initial step size  $d\tau = 0.01/j$ , this algorithm achieves the target accuracy more robustly than fixed-step approaches. In all cases, EH-TEMPO requires far fewer effective evolution steps to construct the full influence functional compared to the layer-by-layer growth required by PT-TEMPO.

Finally, we compare the wall-clock times of EH-TEMPO and PT-TEMPO in Fig. 7. With 4 CPU cores (AMD EPYC 7B13), the computational cost of EH-TEMPO is comparable to that of PT-TEMPO. It should be noted that in the PT-TEMPO implementation, the MPO of the incremental influence functional, whose bond dimension  $M_O$  would be  $7^2 = 49$ ,

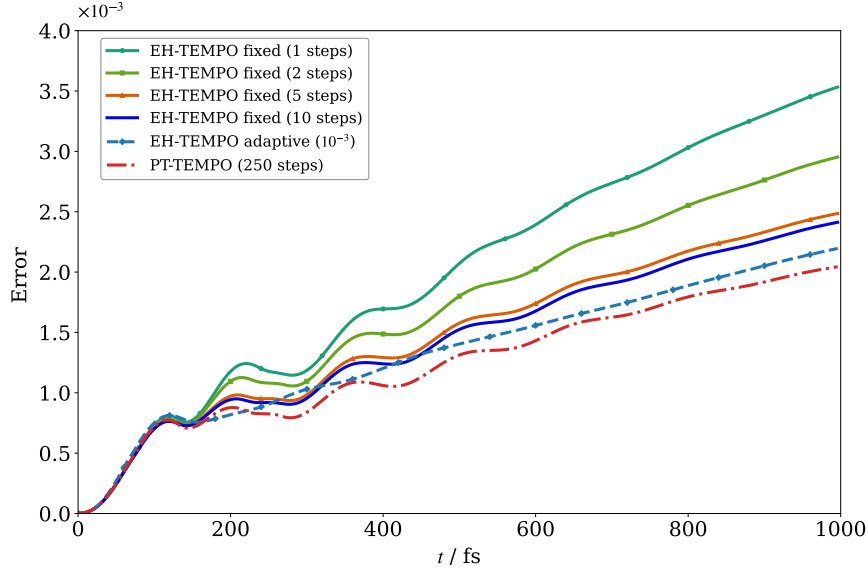


FIG. 6. Convergence analysis of EH-TEMPO with respect to imaginary time evolution step size. The cumulative error  $\mathcal{E}(t)$  is shown for EH-TEMPO using fixed step sizes ( $N_\tau = 1, 2, 5, 10$ ) and an adaptive step-size strategy (relative tolerance  $10^{-3}$ ), compared against the PT-TEMPO reference ( $N_t = 250$ ). Notably, even a single evolution step ( $N_\tau = 1$ ) yields reasonable accuracy, demonstrating the efficiency of the global evolution approach. All calculations used a bond dimension of  $M_S = 60$ .

is decomposed into 7 separate layers of MPOs, each representing one independent bath with  $M_O = 3$ . This decomposition significantly accelerates the PT-TEMPO calculation; without it, simulations with  $M_S = 100$  would be computationally prohibitive. However, since EH-TEMPO avoids large tensor decompositions, it is exceptionally well suited for GPU acceleration. On an NVIDIA A100 GPU, EH-TEMPO achieves speedups of  $2.7\times$ ,  $6.7\times$ , and  $17.5\times$  for bond dimensions  $M_S = 30$ ,  $60$ , and  $100$ , respectively. In contrast, PT-TEMPO, which relies heavily on SVD and QR decompositions—operations that are inherently difficult to parallelize on GPUs—shows limited benefit from GPU acceleration. With GPU, EH-TEMPO can be one order of magnitude faster than PT-TEMPO for  $M_S = 100$ . This makes EH-TEMPO the superior choice for high-accuracy simulations requiring large bond dimensions.

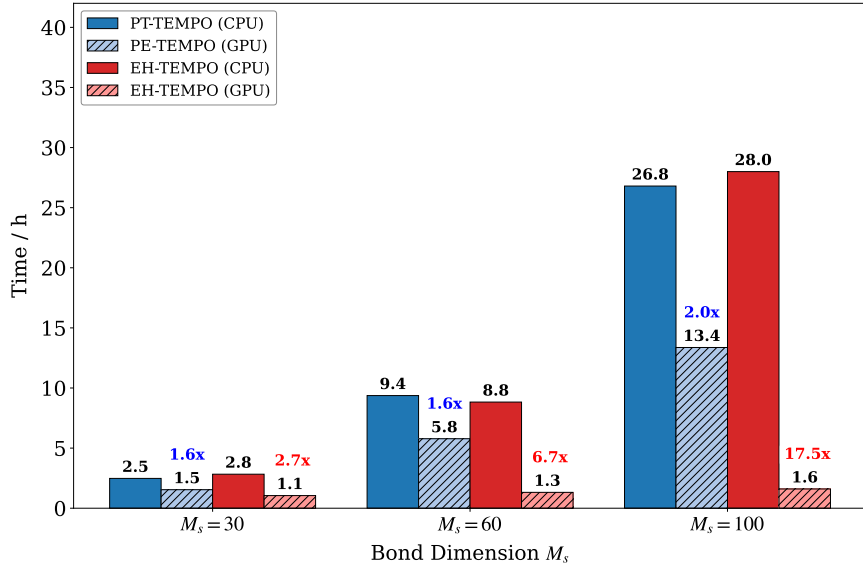


FIG. 7. Computational wall-clock time for the PT-TEMPO and EH-TEMPO algorithms on CPU and GPU platforms as a function of the MPS bond dimension  $M_S$ . The numbers above the bars indicate the specific speedup factor achieved by the GPU implementation relative to the CPU. While CPU performance is comparable between the two methods, EH-TEMPO exhibits superior scalability on GPU hardware, achieving a dramatic  $17.5\times$  speedup at  $M_S = 100$  due to free of large tensor decomposition, compared to the modest gains observed for PT-TEMPO.

#### IV. CONCLUSION

We have introduced the effective Hamiltonian-based time-evolving matrix product operator (EH-TEMPO) algorithm for simulating the non-Markovian dynamics of open quantum systems. The key idea is to reformulate the Feynman-Vernon influence functional as an imaginary time evolution of a one-dimensional effective Hamiltonian with long-range interactions. This mapping naturally casts the effective Hamiltonian into a sum-of-products form, enabling the use of automated, optimal MPO construction algorithms. The most distinctive advantage of EH-TEMPO lies in its scalability. Compared to TEMPO and PT-TEMPO, the computational scaling of EH-TEMPO with respect to the system Hilbert space dimension  $d$  is largely reduced from  $O(d^7)$  to  $O(d^2)$ , by replacing the computationally expensive iterative contraction-and-compression scheme of standard TEMPO and PT-TEMPO with a global imaginary time evolution. Benchmarks on the 7-site Fenna-Matthews-Olson complex demonstrate that EH-TEMPO reproduces the numerically exact population dynamics

obtained from HEOM with high accuracy. A pivotal finding is the intrinsic compressibility of the effective Hamiltonian’s MPO representation: the bond dimensions can be significantly truncated without compromising accuracy, effectively filtering out negligible memory contributions. Furthermore, the backward retrieval scheme allows reconstruction of the full dynamical trajectory from a single one-shot ITE simulation, substantially reducing the computational cost. By circumventing the bottleneck of large tensor decompositions inherent to the original TEMPO algorithm, the method is amenable to massive GPU parallelization. We observed dramatic performance gains on a single GPU, achieving speedups of up to  $17.5\times$  for a typical bond dimension ( $M_S = 100$ ) compared to standard CPU implementations. These results indicate that EH-TEMPO is well positioned to tackle complex multi-state systems that were previously computationally demanding.

## ACKNOWLEDGMENTS

This work is supported by the National Natural Science Foundation of China (Grants 22422301 and 22273005), the Quantum Science and Technology-National Science and Technology Major Project (Grant 2023ZD0300200), and the NSAF (Grant U2330201).

## DATA AVAILABILITY

The data that supports the findings of this study are available within the article.

## REFERENCES

- <sup>1</sup>A. Nitzan, *Chemical dynamics in condensed phases: relaxation, transfer and reactions in condensed molecular systems* (Oxford university press, 2006).
- <sup>2</sup>U. Weiss, *Quantum dissipative systems* (World Scientific, 2012).
- <sup>3</sup>V. May and O. Kühn, *Charge and energy transfer dynamics in molecular systems* (John Wiley & Sons, 2023).
- <sup>4</sup>Y. Yan, Y. Liu, T. Xing, and Q. Shi, “Theoretical study of excitation energy transfer and nonlinear spectroscopy of photosynthetic light-harvesting complexes using the nonperturbative reduced dynamics method,” Wiley Interdiscip Rev Comput Mol Sci **11**, e1498 (2021).

<sup>5</sup>S. J. Jang and B. Mennucci, “Delocalized excitons in natural light-harvesting complexes,” Rev. Mod. Phys. **90**, 035003 (2018).

<sup>6</sup>M. Xu, V. Vadimov, J. Stockburger, and J. Ankerhold, “Colloquium: Simulating non-markovian dynamics in open quantum systems,” Rev. Mod. Phys. , – (2026).

<sup>7</sup>H. Ma, Z. Luo, and Y. Yao, “The time-dependent density matrix renormalisation group method,” Mol. Phys. **116**, 854–868 (2018).

<sup>8</sup>J. Ren, W. Li, T. Jiang, Y. Wang, and Z. Shuai, “Time-dependent density matrix renormalization group method for quantum dynamics in complex systems,” Wiley Interdiscip Rev Comput Mol Sci **12**, e1614 (2022).

<sup>9</sup>F. A. Schröder, D. H. Turban, A. J. Musser, N. D. Hine, and A. W. Chin, “Tensor network simulation of multi-environmental open quantum dynamics via machine learning and entanglement renormalisation,” Nat. Commun. **10**, 1062 (2019).

<sup>10</sup>W. Li, J. Ren, H. Yang, H. Wang, and Z. Shuai, “Optimal tree tensor network operators for tensor network simulations: Applications to open quantum systems,” J. Chem. Phys. **161**, 054116 (2024).

<sup>11</sup>H. Wang and M. Thoss, “Multilayer formulation of the multiconfiguration time-dependent hartree theory,” J. Chem. Phys. **119**, 1289–1299 (2003).

<sup>12</sup>H. Wang, “Multilayer multiconfiguration time-dependent hartree theory,” J. Phys. Chem. A **119**, 7951–7965 (2015).

<sup>13</sup>G. Lindblad, “On the generators of quantum dynamical semigroups,” Communications in mathematical physics **48**, 119–130 (1976).

<sup>14</sup>V. Gorini, A. Kossakowski, and E. C. G. Sudarshan, “Completely positive dynamical semigroups of n-level systems,” Journal of Mathematical Physics **17**, 821–825 (1976).

<sup>15</sup>A. G. Redfield, “On the theory of relaxation processes,” IBM Journal of Research and Development **1**, 19–31 (1957).

<sup>16</sup>A. G. Redfield, “The theory of relaxation processes,” in *Advances in Magnetic and Optical Resonance*, Vol. 1 (Elsevier, 1965) pp. 1–32.

<sup>17</sup>Y. Tanimura and R. Kubo, “Time evolution of a quantum system in contact with a nearly gaussian-markoffian noise bath,” Journal of the Physical Society of Japan **58**, 101–114 (1989).

<sup>18</sup>Y. Tanimura, “Numerically “exact” approach to open quantum dynamics: The hierarchical equations of motion (heom),” J. Chem. Phys. **153**, 020901 (2020).

<sup>19</sup>L. Diósi, N. Gisin, and W. T. Strunz, “Non-markovian quantum state diffusion,” *Phys. Rev. A* **58**, 1699 (1998).

<sup>20</sup>D. Suess, A. Eisfeld, and W. T. Strunz, “Hierarchy of stochastic pure states for open quantum system dynamics,” *Phys. Rev. Lett.* **113**, 150403 (2014).

<sup>21</sup>N. Makri and D. E. Makarov, “Tensor propagator for iterative quantum time evolution of reduced density matrices. i. theory,” *J. Chem. Phys.* **102**, 4600–4610 (1995).

<sup>22</sup>N. Makri and D. I. Makarov, “Tensor propagator for iterative quantum time evolution of reduced density matrices. ii. numerical methodology,” *J. Chem. Phys.* **102**, 4611–4618 (1995).

<sup>23</sup>N. Makri, “Improved feynman propagators on a grid and non-adiabatic corrections within the path integral framework,” *Chem. Phys. Lett.* **193**, 435–445 (1992).

<sup>24</sup>N. Makri, “Quantum dissipative dynamics: A numerically exact methodology,” *J. Phys. Chem. A* **102**, 4414–4427 (1998).

<sup>25</sup>A. Strathearn, P. Kirton, D. Kilda, J. Keeling, and B. W. Lovett, “Efficient non-markovian quantum dynamics using time-evolving matrix product operators,” *Nat. Commun.* **9**, 3322 (2018).

<sup>26</sup>E. Ye and G. K.-L. Chan, “Constructing tensor network influence functionals for general quantum dynamics,” *J. Chem. Phys.* **155**, 044104 (2021).

<sup>27</sup>M. Cygorek, M. Cosacchi, A. Vagov, V. M. Axt, B. W. Lovett, J. Keeling, and E. M. Gauger, “Simulation of open quantum systems by automated compression of arbitrary environments,” *Nat. Phys.* **18**, 662–668 (2022).

<sup>28</sup>U. Schollwöck, “The density-matrix renormalization group in the age of matrix product states,” *Ann. Phys.* **326**, 96–192 (2011).

<sup>29</sup>M. R. Jørgensen and F. A. Pollock, “Exploiting the causal tensor network structure of quantum processes to efficiently simulate non-markovian path integrals,” *Phys. Rev. Lett.* **123**, 240602 (2019).

<sup>30</sup>M. Richter and S. Hughes, “Enhanced tempo algorithm for quantum path integrals with off-diagonal system-bath coupling: Applications to photonic quantum networks,” *Phys. Rev. Lett.* **128**, 167403 (2022).

<sup>31</sup>D. Gribben, D. M. Rouse, J. Iles-Smith, A. Strathearn, H. Maguire, P. Kirton, A. Nazir, E. M. Gauger, and B. W. Lovett, “Exact dynamics of nonadditive environments in non-markovian open quantum systems,” *PRX Quantum* **3**, 010321 (2022).

<sup>32</sup>S. Zhang and Q. Shi, “Time-evolving matrix product operator method in a nondiagonal basis set based on the derivative of the path-integral expression,” *Phys. Rev. A* **111**, 062210 (2025).

<sup>33</sup>A. Bose, “Quantum correlation functions through tensor network path integral,” *J. Chem. Phys.* **159**, 214110 (2023).

<sup>34</sup>N. Ng, G. Park, A. J. Millis, G. K.-L. Chan, and D. R. Reichman, “Real-time evolution of anderson impurity models via tensor network influence functionals,” *Phys. Rev. B* **107**, 125103 (2023).

<sup>35</sup>R. Chen, X. Xu, and C. Guo, “Grassmann time-evolving matrix product operators for quantum impurity models,” *Phys. Rev. B* **109**, 045140 (2024).

<sup>36</sup>N. Makri, “Small matrix disentanglement of the path integral: overcoming the exponential tensor scaling with memory length,” *J. Chem. Phys.* **152** (2020).

<sup>37</sup>S. Kundu and N. Makri, “Pathsum: A c++ and fortran suite of fully quantum mechanical real-time path integral methods for (multi-) system+ bath dynamics,” *J. Chem. Phys.* **158**, 224801 (2023).

<sup>38</sup>A. Bose and P. L. Walters, “A multisite decomposition of the tensor network path integrals,” *J. Chem. Phys.* **156**, 024101 (2022).

<sup>39</sup>C. Hubig, I. McCulloch, and U. Schollwöck, “Generic construction of efficient matrix product operators,” *Phys. Rev. B* **95**, 035129 (2017).

<sup>40</sup>J. Ren, W. Li, T. Jiang, and Z. Shuai, “A general automatic method for optimal construction of matrix product operators using bipartite graph theory,” *J. Chem. Phys.* **153** (2020).

<sup>41</sup>H. Çakır, R. M. Milbradt, and C. B. Mendl, “Optimal symbolic construction of matrix product operators and tree tensor network operators,” *Phys. Rev. B* **112**, 035101 (2025).

<sup>42</sup>J. Haegeman, C. Lubich, I. Oseledets, B. Vandereycken, and F. Verstraete, “Unifying time evolution and optimization with matrix product states,” *Phys. Rev. B* **94**, 165116 (2016).

<sup>43</sup>W. Li, J. Ren, and Z. Shuai, “Numerical assessment for accuracy and gpu acceleration of td-dmrg time evolution schemes,” *J. Chem. Phys.* **152**, 024127 (2020).

<sup>44</sup>J. Shao and N. Makri, “Iterative path integral calculation of quantum correlation functions for dissipative systems,” *Chem. Phys.* **268**, 1–10 (2001).

<sup>45</sup>J. Shao and N. Makri, “Iterative path integral formulation of equilibrium correlation functions for quantum dissipative systems,” *J. Chem. Phys.* **116**, 507–514 (2002).

<sup>46</sup>R. P. Feynman and F. Vernon Jr, “The theory of a general quantum system interacting with a linear dissipative system,” *Ann. Phys.* **281**, 547–607 (2000).

<sup>47</sup>L. Liu, J. Ren, and W. Fang, “Improved memory truncation scheme for quasi-adiabatic propagator path integral via influence functional renormalization,” *J. Chem. Phys.* **161**, 084101 (2024).

<sup>48</sup>A. Ishizaki and G. R. Fleming, “Theoretical examination of quantum coherence in a photosynthetic system at physiological temperature,” *Proc. Natl. Acad. Sci.* **106**, 17255–17260 (2009).

<sup>49</sup>J. Adolphs and T. Renger, “How proteins trigger excitation energy transfer in the fmo complex of green sulfur bacteria,” *Biophys. J.* **91**, 2778–2797 (2006).